Ocean Engineering 243 (2022) 110272

Contents lists available at ScienceDirect

Ocean Engineering

journal homepage: www.elsevier.com/locate/oceaneng

Investigation of fine viscous flow fields in ship planar motion mechanism tests by DDES and RANS methods

Zhen Ren, Jianhua Wang, Decheng Wan *

Computational Marine Hydrodynamics Lab (CMHL), School of Naval Architecture, Ocean and Civil Engineering, Shanghai Jiao Tong University, Shanghai 200240, China

ARTICLE INFO

Keywords:
Planar motion mechanism
DDES
RANS
Vortex identification method
Vortex structure
Liutex
Naoe-FOAM-SJTU solver

ABSTRACT

The fine large separated flow is a focus in the naval architecture and ocean engineering. In the present study, the CFD solver, naoe-FOAM-SJTU, coupled with delayed detached-eddy simulation (DDES) and Reynolds Averaged Navier-Stokes (RANS) is adopted to simulate the fine viscous flow field in the ship planar motion mechanism (PMM) tests for the benchmark model Yupeng Ship. This paper compares the time histories of forces/moment acting on the hull and their oscillation frequency obtained by Fast Fourier Transform. The predicted results are in good agreement with the experimental data. By comparing the turbulent kinetic energy (TKE) and eddy viscosity coefficient calculated by both numerical methods, the results show that the TKE and eddy viscosity coefficient obtained by DDES method are much less than that achieved by RANS approach. The capacity of four vortex identification methods to capture vortex structures is analyzed in this paper, indicating that the third generation of vortex identification methods (Ω_R and Liutex methods) are more suitable for analyzing the flow mechanism in the viscous large separated flow field. The axial Liutex and streamlines on the cutting planes are used to depict the flow around the hull.

1. Introduction

Planar motion mechanism (PMM) tests are a kind of typical hydrodynamic tests to evaluate the hydrodynamic derivatives and analyze the flow mechanism in the large separated flow around the hull. Extensive studies are conducted worldwide to analyze the viscous flow field of the hull by experiments and computational fluid dynamics (CFD). As an increasing popular method on the ship hydrodynamics, CFD based viscous flow theory can provide much details in the flow field to facilitate the analysis of flow mechanism around the hull. Researchers have developed many CFD solvers such as CFDShip-Iowa, naoe-FOAM-SJTU, based on the viscous flow theory.

Simonsen and Stern (2005) simulated the viscous flow field of Esso Osaka ship with full appendages by using the self-developed the solver, CFDShip-Iowa. In their studies, the vortex structures around the hull are analyzed to reveal the flow mechanism in the static drift tests. Xing et al. (Xing, 2007; Xing et al., 2010, 2012) conducted the numerical simulations for the static drift tests of KVLCC2 at drift angle 0, 12, 30 and 60° by the blended k-ε/k-ω (BKW) RANS models and BKW-DES (Detached-eddy simulation). Ohashi and Hino (2009) used RANS, DES and DDES methods to analyze the flow mechanism behind a cylinder wall. It was found that DES/DDES approaches were more suitable for simulating the large separated flows. In addition, DDES and RANS approaches were applied to capture the bow wave breaking by Wang (Wang et al., 2020) and Ren (Ren et al., 2018). In their studies, DDES approach was able to capture more scars and plunging wave breaking. Kandasamy (Kandasamy et al., 2009) and Xing (Xing and Stern, 2007) et al. studied the large-scale unsteady vortex structures around a hydrofoil NACA0024 piercing the free surface by DES and RANS methods. For analyzing the flow mechanism of the hull at different angle, Pinto-Heredero et al. (2010) used the self-developed CFD solver, CFDShip-Iowa, to simulate the viscous flow field of Wigley hull. The relationship between the vortex structures and Kelvin wave pattern was revealed in their study. Bhushan et al. (Bhushan et al., 2012) used the DES method to simulate the viscous flow field of appended Athena in full scale conditions. They explained the dominant frequency of transom flow by vortical structures and associated instabilities. The complex vortex structures around a propeller were studied by Heydari and Sadat-Hosseini (2020).

As for PMM tests of the hull, extensive studies were conducted by researchers such as Sakamoto et al., 2012a, 2012b and Yoon et al.,

* Corresponding author.
E-mail address: dcwan@sjtu.edu.cn (D. Wan).
URL: https://dcwan.sjtu.edu.cn/ (D. Wan).

https://doi.org/10.1016/j.oceaneng.2021.110272
Received 22 July 2021; Received in revised form 21 November 2021; Accepted 26 November 2021
Available online 3 December 2021

2015a, 2015b. They conducted the numerical simulations of the static drift tests, dynamic pure sway and yaw tests of DTMB5415. The predicted hydrodynamic derivatives were in good agreement with the experimental results. In their studies, they deeply analyzed the viscous flow field such as the wave generation and the vorticity field around the hull. Meng and Wan (2016) studied the effect of water depth on the hydrodynamic performance of KLVCC2M in static drift tests.

So far, PMM tests are usually used to analyze the hydrodynamic derivatives of ships, not the flow mechanism in the viscous flow field around the hull. In this paper, the DDES and RANS approaches are applied to simulate the complex viscous flow field of PMM tests for Yupeng ship. The self-developed CFD solver, naoe-FOAM-SJTU, is used in the present simulations. Four vortex identification methods are adopted to capture the vortex structures, and the flow mechanism around the hull is depicted by Liutex vector and streamlines. Next is the framework of this paper. The first part is the numerical methods including RANS and DDES method. The second part is the geometry model of Yupeng ship, test conditions and grid generation in the present numerical simulations. The results show the forces/moment, free surface, vortex structures, axial Liutex and streamline. Finally, the conclusion of this paper is drawn.

2. Numerical approach

2.1. Basic numerical schemes

The CFD solver, naoe-FOAM-SJTU (Shen et al., 2015; Wang and Wan, 2016; Wang et al., 2017), is developed based on the open-source code platform OpenFOAM. The basic governing equations (RANS) contain the mass conservation equation and the moment conservation equation. A high-resolution volume of fluid (VOF) (Berberović et al., 2009) is adopted to capture the free surface. The turbulence mode, shear stress transport (SST) k-ω model (Menter et al., 2003), is selected to solve Reynold stress.

The delayed detached-eddy simulation (DDES) is the modification of basic DES method by redefining the turbulent length scale, l_{DDES}, which can avoid the RANS calculation area being switched to LES mode too early.

$$l_{DDES} = l_{RANS} - f_d \max(0, l_{RANS} - C_{DES}\Delta) \tag{1}$$

where f_d is the empirical blending function defined as

$$f_d = 1 - \tanh\left[(C_{d1} r_d)^{C_{d2}}\right] \tag{2}$$

$$r_d = \frac{\nu_t + \nu}{\kappa^2 d_w^2 \sqrt{0.5\left(S^2 + \Omega^2\right)}} \tag{3}$$

where, ν_t is the eddy viscosity and ν represents the molecular viscosity. κ is the von Karman constant. d_w is the distance to wall. The implementation of the DDES approach in the naoe-FOAM-SJTU solver can be referred in the literatures (Zhao and Wan, 2016; Zhao et al., 2018).

The finite volume method (FVM) with multi-unstructured overlapping grids is adopted to discretize the computational domain in space. For decoupling the pressure-velocity equations in governing equations, the PIMPLE algorithm combining the pressure implicit splitting operator (PISO) and semi-implicit method for pressure-linked equations (SIMPLE) is selected since it is more suitable for strongly nonlinear two-phase flow solution. Several built-in discretized schemes in OpenFAM are applied to solve the partial differential equations (PDE). The convection term in momentum equation is discretized by the second-order total variation diminishing (TVD) limited linear scheme. The viscous terms are solved by a second-order central difference scheme. Excepting for the implicit Euler scheme solving VOF advection equation, the second-order backward scheme is applied for temporal discretization. In the postprocessing, the third generation of vortex identification methods including Ω_{R} method and Liutex vector are applied to capture the vortex structures and vortex vector around the hull. The results are compared with the vortex structures based-vorticity (first generation) and Q-criteria (second generation).

2.2. Overset grid method

The dynamic overset grid technology (Shen et al., 2015) is applied for the large amplitude motion in the PMM tests. In the present simulations, the background grid and hull grid are respectively generated by commercial software, HEXPRESS. Fig. 1 shows the assembling process of multiple sets of grids in overset grid. Fig. 1 (a) presents the grid distribution before assembling. Red represents the background grid and blue is the hull grid. After assembling, the background grid cells in the boundary of hull grid are cleared. And there is an obvious overlapping region around the hull grid. Donor cells are the cells who is responsible for providing flow field information to fringe cells. Active cells are the unit that participates in normal calculations. Their values directly reflect the actual flow field.

2.3. Vortex identification method

The Liutex/Rortex vector method proposed by Liu (Liu et al., 2019) systematically solves the problem that proposes the rotating part of the rigid body from the fluid motion. The Liutex/Rortex vector method is introduced from the following two aspects: the direction problem of Liutex/Rortex vector and the size of the Liutex/Rortex vector.

Firstly, the velocity gradient tensor ∇V and its eigenvalues are solved in geodetic coordinate system. If the eigenvalues of the velocity gradient tensor include a real one λ_r and two conjugate complex values $\lambda_{cr} \pm \lambda_{ci}$, the eigenvector $\boldsymbol{v}_r$ corresponding to the real eigenvalue is only stretched or compressed in direction. The rotation can only occur in the plane perpendicular to the real eigenvector $\boldsymbol{v}_r$, which is the rotation axis of the local fluid elements. The direction vector $\boldsymbol{r}$ of the Liutex vector is $\boldsymbol{v}_r$. It should be noted that both $\boldsymbol{v}_r$ and $-\boldsymbol{v}_r$ are the real eigenvector of λ_r. The direction $\boldsymbol{r}$ of Liutex vector is uniquely determined by definition $\langle \boldsymbol{\omega}, \mathbf{r} \rangle > 0$.

The Liutex vector represents the rigid rotation part in the motion of fluid element. In order to solve the size R of Liutex vector, the initial xyz coordinate system is rotated to $x_Q y_Q z_Q$ by Q rotation that make the z_Q after rotation is in the same direction as the rotation axis $\boldsymbol{r}$. The velocity gradient tensor after rotation becomes:

$$\nabla V_Q = Q \nabla V Q^T = \begin{bmatrix} \dfrac{\partial u_Q}{\partial x_Q} & \dfrac{\partial u_Q}{\partial y_Q} & 0 \\ \dfrac{\partial v_Q}{\partial x_Q} & \dfrac{\partial v_Q}{\partial y_Q} & 0 \\ \dfrac{\partial w_Q}{\partial x_Q} & \dfrac{\partial w_Q}{\partial y_Q} & \dfrac{\partial w_Q}{\partial z_Q} \end{bmatrix} \tag{4}$$

where Q is the rotation matrix while u, v and w represent the velocity components in the xyz coordinate.

And then, a second rotation (P rotation) is used to rotate the reference frame around the z-axis

$$P = \begin{bmatrix} \cos\theta & \sin\theta & 0 \\ -\sin\theta & \cos\theta & 0 \\ 0 & 0 & 1 \end{bmatrix} \tag{5}$$

and the corresponding velocity gradient tensor

$$\nabla V_\theta = P \nabla V_Q P^T \tag{6}$$

The rotational strength is defined as twice the minimal absolute value of the off-diagonal component of the 2×2 upper left submatrix and is given by:

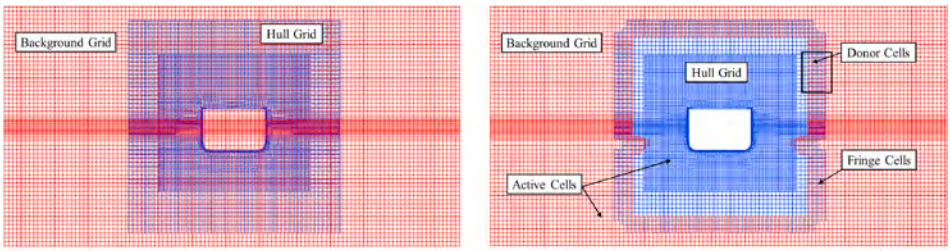

(a) Original distribution of the computational grid (b) Final distribution of the computational grid

Fig. 1. Assembling process of overlapping grid.

$$R = \begin{cases} 2(\beta - \alpha), & \alpha^2 - \beta^2 < 0 \\ 0, & \alpha^2 - \beta^2 \geq 0 \end{cases} \tag{7}$$

where

$$\alpha = \frac{1}{2}\sqrt{\left(\frac{\partial v_Q}{\partial y_Q} - \frac{\partial u_Q}{\partial x_Q}\right)^2 + \left(\frac{\partial v_Q}{\partial x_Q} + \frac{\partial u_Q}{\partial y_Q}\right)^2} \tag{8}$$

$$\beta = \frac{1}{2}\left(\frac{\partial v_Q}{\partial x_Q} - \frac{\partial u_Q}{\partial y_Q}\right) \tag{9}$$

The Liutex/Rortex can be defined as

$$\mathbf{R} = \left(\langle \boldsymbol{\omega}, \mathbf{r} \rangle - \sqrt{\langle \boldsymbol{\omega}, \mathbf{r} \rangle^2 - 4\lambda_{ci}^2}\right)\mathbf{r} \tag{10}$$

Newly, the Omega-Liutex method Ω_R is proposed by combing omega and Liutex/Rortex methods.

$$\Omega_R = \frac{\beta^2}{\alpha^2 + \beta^2 + \varepsilon} \tag{11}$$

where ε is a small positive parameter to remove non-physical noises.

3. Numerical simulation setup

3.1. Geometry model

The benchmark ship model, Yupeng Ship with L_{pp} being 3.857 m, is selected to study the viscous flow field in the PMM tests. Its geometry and principal particulars are presented in Fig. 2 and Table 1. Extensive experiments are performed in the towing tank of Marine design and Research Institute of China (MARIC). The PMM experiment schemes are made by them according to the ITTC rules. The experiment schemes are similar to the PMM tests of Derradji-Aouat (Derradji-Aouat and Thiel, 2004), as shown in Fig. 3. In the experiments and present study, the speed is 1.323 m/s with heave and pitch being taken into consideration. The PMM tests are designed for studying the maneuverability of Yupeng ship, focusing on the amplitude of lateral force and yawing moment. The relevant experiments belong to the projects of China Numerical Tank and are not published until now.

3.2. Tests conditions

The PMM tests include the static drift test, dynamic pure sway and yaw tests, which are summarized in Table 2. In the present simulations, larger drift angel and shorter period are selected to analyze the evolution of the viscous flow field in large-separated flow. Fig. 4 shows the local coordinate system. *oxyz* represents the local coordinate system where the origin is at the center of gravity of the ship model.

Fig. 2. Geometry model of Yupeng Ship.

Table 1
Principal particulars of Yupeng Ship.

Main particulars	Symbols	Unit	Value
Length between perpendiculars	L_{pp}	m	3.857
Beam	B_{WL}	m	0.567
Draft	T_M	m	0.210
Block coefficient	*CB*		0.721
Longitudinal inertial radius	*Ryy*	m	0.984
Fr	-	–	0.215
Re	-	–	4.60×10^6

Fig. 3. Planar Motion Mechanism (PMM) test setup (Derradji-Aouat and Thiel, 2004).

Table 2
Summary of tests and calculated conditions.

Conditions	Amplitude(m)	Period(s)	Drift angle (°)
Static drift test (S.D.)	–	–	20
Pure sway test (P.S.)	0.4	8	–
Pure yaw test (P.Y.)	0.4	8	–

3.3. Grid generation and uncertainty analysis

3.3.1. Grid generation

In the present simulations, the grid is generated by commercial software, HEXPRESS. The arrangement of grid is referred the literature [27] where the mesh independency is completed. Fig. 5 presents the computational domain and boundary conditions in the current simulation. Both blocks are adopted to refine the local flow field and free

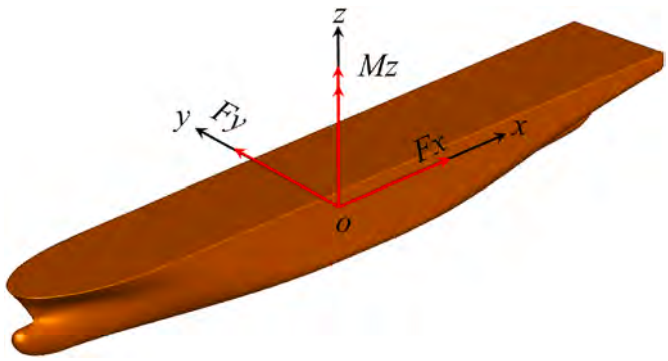

Fig. 4. Coordinate system of force and moment.

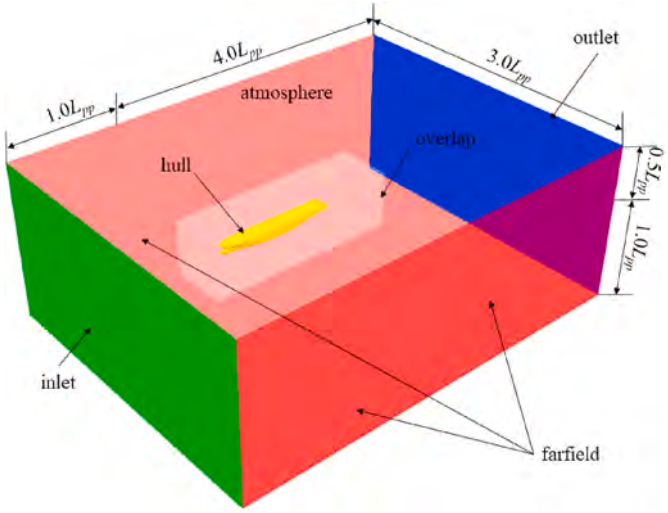

Fig. 5. Computational domain and boundary condition.

surface. The origin of the coordinates is set at the intersection of the waterline and the bow perpendicular. The direction of x-axis is from the bow of the hull to the stern and the y-axis is positive to starboard with z-axis pointing upward. The range of computational domain in three directions are: $-1.0L_{PP} < x < 4.0L_{PP}$, $-1.5L_{PP} < y < 1.5L_{PP}$, $-1.0L_{PP} < z < 0.5L_{PP}$. In the present simulations, three sets of systematically refined grids with a refinement ratio being $\sqrt{2}$ are adopted to analyze the mesh independency. The grid arrangement in these three sets is summarized in Table 3. And the grid distribution on the longitudinal planes is shown in Fig. 6. The red line represents the background grid distribution and the blue is the hull.

3.3.2. Grid uncertainty

To ensure the reliability of the present simulations, the grid uncertainty of predicted resistance in static drift test using RANS method is analyzed according to the ITTC recommended procedures. The predicted resistance by three sets grids is listed in Table 4.

The convergence ratio RG can be written as:

$$R_G = \varepsilon_{21}/\varepsilon_{32} \tag{12}$$

Table 3
Details of mesh generation.

Grid sets	Background Mesh (Million)	Hull Mesh (Million)	Total (Million)
Coarse	0.77	1.47	2.24
Mid	2.16	4.12	8.28
Fine	6.05	11.54	17.59

where $\varepsilon_{21} = S_2 - S_1$ and $\varepsilon_{32} = S_3 - S_2$. S_1, S_2, S_3 represent the solutions on the fine, medium and coarse mesh, respectively. According to ITTC, three convergence situations are possible:

(1) Monotonic convergence: $0 < R_G < 1$
(2) Oscillatory convergence: $R_G < 0$
(3) Divergence: $R_G > 0$

The value of R_G in this study is 0.507 and meets the criteria (1). Based on the Richardson Extrapolation (RE), the error can be expressed as follows:

$$\delta_{\mathrm{RE}} = \frac{\varepsilon_{21}}{r_G^{P_G} - 1} \tag{13}$$

where the r_G is the grid refinement ratio $\sqrt{2}$ and P_G is the observed order of accuracy in the present simulations, the expression of P_G is:

$$P_G = \frac{\ln(\varepsilon_{32}/\varepsilon_{21})}{\ln(r_G)} \tag{14}$$

Besides, the correction factor can be expressed as:

$$C_G = \frac{r_G^{P_G} - 1}{r_G^{P_{Gest}} - 1} \tag{15}$$

where the P_{Gest} is an estimate for the limiting order of accuracy as the spacing size goes to zero and its value is 2 in this work. Finally, the grid uncertainty can be written as follows:

$$U_G = \begin{cases} \left[9.6(1-C_G)^2 + 1.1\right]|\delta_{\mathrm{RE}}|, & |1-C_G| < 0.125 \\ \left[2\ |1-C_G| + 1\right]|\delta_{\mathrm{RE_{i,1}}}|, & |1-C_G| \geq 0.125 \end{cases} \tag{16}$$

Table 5 shows the values of R_G, P_G, δ_{RE}, C_G and U_G. The observed order of accuracy P_G is 1.961 and is very close to the theoretical order of accuracy P_{Gest}. The error estimated by RE is less than 3% of S1, indicating that the current numerical simulation is well convergent. The correction factor C_G is 0.973 and according to the ITTC procedures, the grid uncertainty is 2.87% of the experimental data.

4. Results and discussion

In the present study, all the numerical simulations are performed on the High-performance computing cluster in Computational Marine Hydrodynamic Lab (CMHL), Shanghai Jiao Tong University. The simulations in this paper are carried out by the self-developed CFD solver, naoe-FOAM-SJTU. In the numerical simulations, each case needs 40 cores that 39 cores are used to calculate the viscous flow field of PMM and one core is for the interpolation calculation of overset grids. With the Courant number being less than 1, the time step is equal to 0.0005s. Each case using RANS method needs approximately 224 h and the other case (DDES method) costs 316 h. The results at last two periods in the numerical simulations are adopted in the postprocessing.

4.1. Static drift test

4.1.1. Force and moments

The predicted accuracy of hydrodynamic performance is crucial to the numerical simulation of ship maneuverability. The predicted force/moment are compared with the experimental data, as shown in Fig. 7. Table 6 summarizes the comparison between the predicted and experimental results. The forces and moment are the averaged value in the time histories. In terms of resistance, the results are underestimated by both numerical methods. Since the PMM tests mainly focus the lateral force and yawing moment, the range of the dynamometer used to measure the force is quite large, inducing the large pulsation characteristics of the time histories. In addition, the resistance in PMM tests is less relative to the lateral force and yawing moment, which also makes it

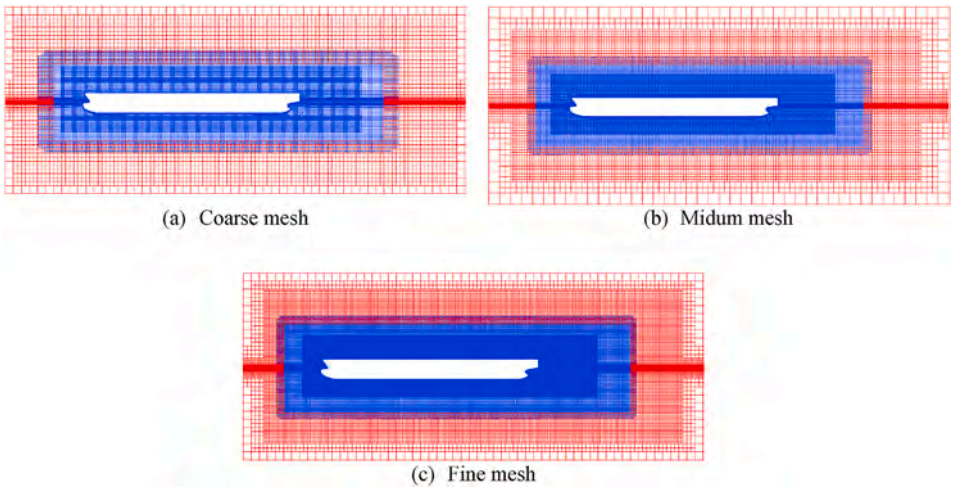

Fig. 6. Grid distribution with different resolutions.

Table 4
Predicted resistance by three sets of grids.

Item	EFD (D)	Coarse (S3)	Medium (S2)	Fine (S1)
Value	15.08	13.02	13.77	14.15
Error	–	−13.66%	−8.69%	−6.18%

Table 5
Values of R_G, P_G, δ_{RE}, C_G and U_G.

R_G	P_G	$\delta_{RE}\%S_1$	C_G	$U_G\%D$
0.507	1.961	2.76	0.973	2.87

difficult to accurately measure the resistance. Due to the great fluctuation of the measured resistance during the experiment, the error of resistance is large. The lateral force is more over-predicted by DDES method than RANS approach and its error is larger than 10%. According to the results in Table 6, yawing moment obtained by DDES method is in best agreement with the experimental data. Overall, the oscillation period of predicted lateral force and yawing moment obtained by both methods are basically the same. As shown in Fig. 7, the time histories of resistance, lateral force and yawing moment are periodic and the period and amplitude are also irregular. This is because that the range of the dynamometer is large and the velocity of the trailer in the experiments is pulsatile, leading to the irregular fluctuations of measured forces/moment. But in the numerical simulations, the stability of ship speed can

Table 6
Comparison between the predicted and experimental forces and moment in static drift test.

Force/moment	EFD	CFD			
		RANS	Error	DDES	Error
Mean of resistance (N)	15.08	13.85	−7.88%	13.68	−9.04%
Mean of lateral force (N)	81.66	86.66	6.12%	89.98	10.20%
Mean of yawing moment (NM)	127.80	120.21	−5.89%	122.34	−4.22%

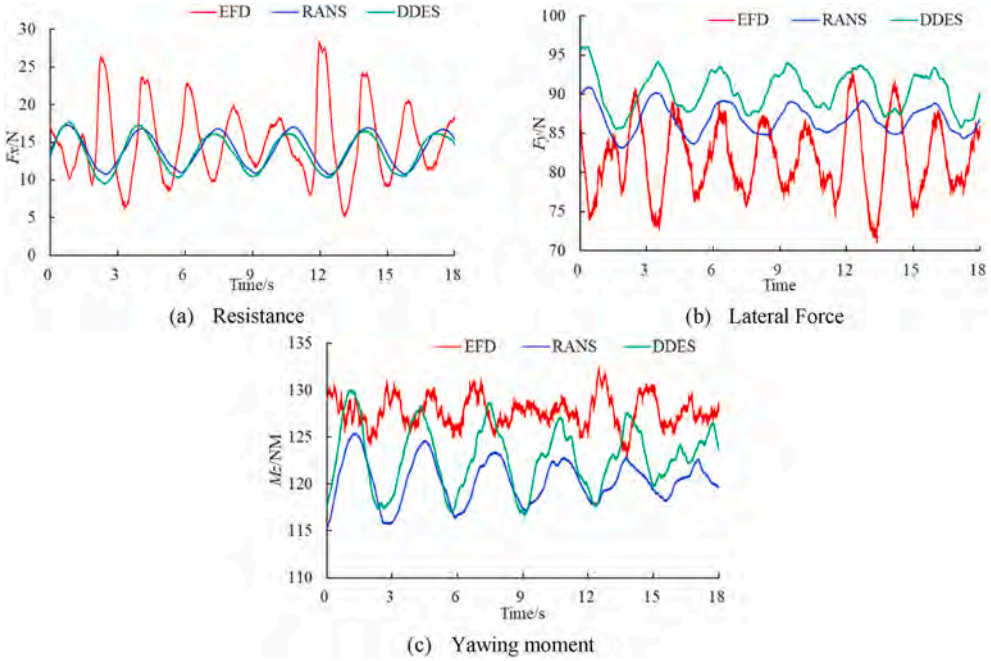

Fig. 7. Time histories of forces and moments (a: resistance; b: lateral force; c: yawing moment).

be absolutely guaranteed. The regular and periodic oscillation of forces and moment are induced by the numerical oscillation in the solution of free surface by VOF method.

4.1.2. Free surface

Although the wave pattern of free surface is not provided in the experiments, the results achieved by DDES and RANS methods are shown in Fig. 8. The distribution of turbulent kinetic energy and eddy viscosity coefficients are also displayed in Fig. 8. As shown in Fig. 8 (a), asymmetric Kelvin wave pattern is captured by both numerical approaches. The plunging wave breaking is also investigated near the bow on the portside. It is found that the free surface captured by RANS approach is smoother than that in the simulations based DDES method. This is the inevitable result of time averaging in RANS method.

Turbulent kinetic energy is closely related to turbulence intensity and eddy viscosity coefficient reflects the stress produced by turbulent flow. By comparing the distribution of TKE obtained by both methods, it is found that although the regions with large turbulent kinetic energy obtained by both methods are near the bow and stern, the turbulent kinetic energy obtained by DDES method is much less than that by RANS approach. Higher TKE indicates that stronger turbulent flow occurs near the bow and stern, indicating that there are large scale and strong vortex structures. Fig. 8 (b) shows the evolution region of TKE calculated by DDES method is larger than the results from RANS approach on both side of the hull, which indicates that turbulence in the simulation with DDES method develops further in the far-field. The TKE achieved by RANS approach decays rapidly during the development to the far field flow, indicating that the turbulent flow is rapidly averaged in the far flow field. The smoother velocity field is calculated by RANS method, which cannot reflect the real flow field. But DDES approach can simulate the turbulent flow and pulsating velocity distribution in the far field more accurately.

As investigated in Fig. 8 (c), there is an order of magnitude difference between the prediction results of DDES and RANS methods. The maximum of eddy viscosity coefficient obtained by DDES method is 4.28e-4, while the maximum achieved by RANS approach reaches 6.35e-3. RANS method overestimates the eddy viscosity in the flow field, leading to the serious turbulent flow dissipation and less velocity in the flow field. This result presented by RANS method is not reasonable. Being like the distribution of turbulent kinetic energy, the value of eddy viscosity coefficient in the DDES simulation is larger than zero in far-field. In the numerical simulation of RANS approach, the distribution of eddy viscosity is relatively concentrated and varies rapidly. The region with higher value of eddy viscosity coefficient occurs near the bow and stern and its value decreases rapidly during the evolution to starboard and portside. This distribution illustrates that there is serious dissipation near the bow and stern of the hull, resulting in the lower velocity in the wake field. Finally, the predicted resistance by RANS method is larger than that obtained by DDES approach.

4.1.3. Vortex structure

In the present simulations, DDES and RANS methods are used to solve the viscous flow field in the PMM tests of Yupeng Ship. According to the theory of DDES method, SST k-ω turbulence model is used to solve the flow field in the near-wall regions and LES subgrid-scale model is adopted in the other regions. To better investigate the flow field around the hull and compare the behaviors of three generation of vortex identification methods, the vortex structures are obtained by the methods based-vorticity (first generation), Q criteria (second generation) and Ω_R method and Liutex vector (third generation). Since vorticity and Liutex

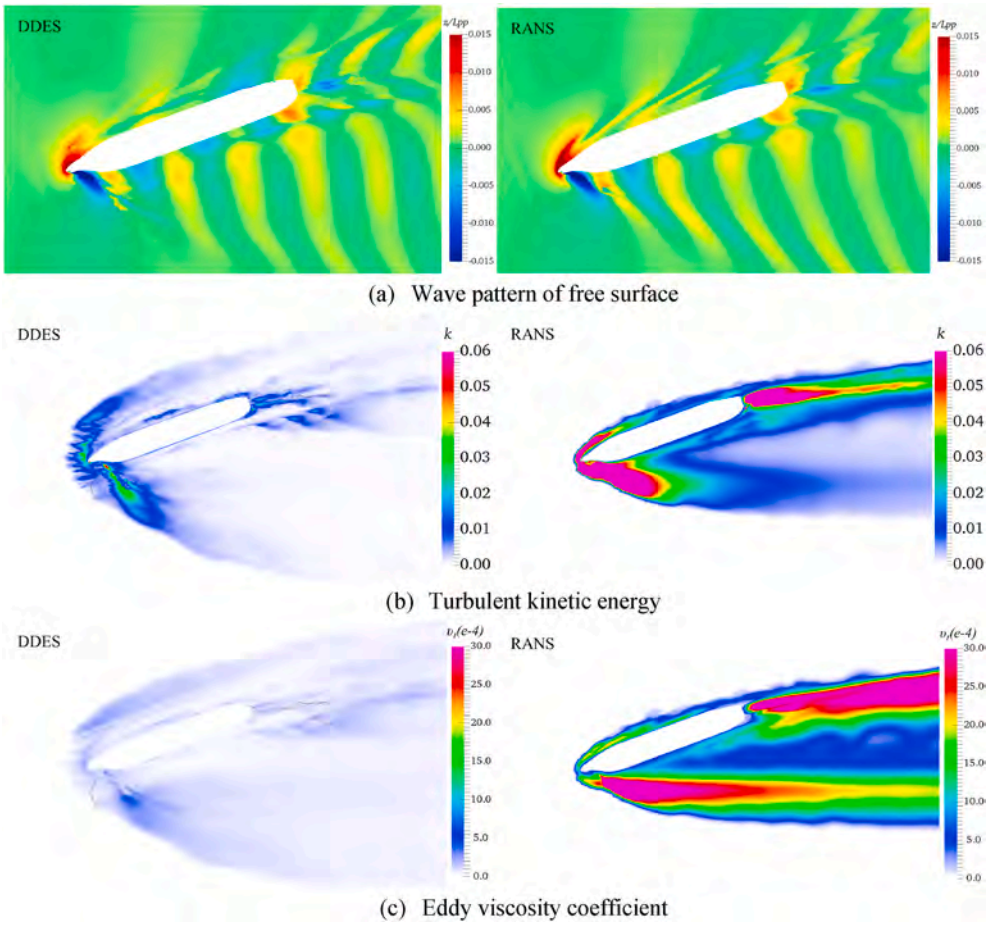

Fig. 8. Wave pattern (a), turbulent kinetic energy(b) and eddy viscosity coefficient (c).

are vectors, the threshold of vortex structure is selected according to the magnitude of vorticity and Liutex vectors. According to the theory, the threshold of Ω_R is not artificially selected and equals to 0.52.

Overall, more vortex structures, as shown in Fig. 9, are investigated in the numerical simulation of DDES method, especially in the regions which are far from the wall. In the current numerical simulations, three main vortex structures are captured by DDES method and RANS approach only makes two main vortex structures visible. The first main vortex structures are captured on the portside of the hull, which start from the bottom of the bow and shed from the hull shoulder. It indicates that separated flow appears near the vortex shedding point from the hull shoulder. The first vortex structures gradually approach free surface as it develops downstream. The second vortex structures mainly originate from the stern and develops downstream along the propeller shaft. The third vortex structures, which are captured by DDES method but not by RANS approach, start from the bow wave on the starboard and merge with the second vortex structures near the stern downstream.

Four vortex identification methods are used to depict vortex structures in the numerical simulations of PMM tests. Fig. 9 (a) depicts the vortex structures obtained by the first generation of vortex identification method based on vorticity. It is obviously unreasonable that the hull is fully covered by the vortex structures. Compared with the vortex structures achieved by RANS approach, large sheet vortex structures on the free surface near the bow are captured by DDES method. The vortex structures identified by *Q*-criteria (second generation) are greatly affected by the artificial selected threshold. In the numerical simulation with DDES method, *Q*-criteria identifies longer main vortex structures and more breaking vortex, as shown in Fig. 9 (b). As one of third generation methods, Ω_R mehtod is used to evaluate the relative strength of vortex in the flow field. As investigated in Fig. 9 (c), Ω_R method can identify more relative strong vortex structures in the viscous flow field. At last, Fig. 9 (d) presents the comparison of vortex structures obtained by Liutex method in the simulations with DDES and RANS methods. DDES method can capture more vortex structures than that with RANS method. Although the vortex structures are more breaking and finer, it better reflects the flow mechanism of viscous flow field according to the uniqueness and accuracy of its definition.

4.1.4. Flow field

After analyzing the evolution of vortex structures in the global flow field, the surface streamlines and axial Liutex on the different cutting planes are presented in this subsection for further studying the flow mechanism. At first, the axial Liutex and streamlines at $x/L_{pp} = 0.10$ near the bow are shown in Fig. 10. This plane is in the region of the bow wave evolution. In the stratic drift tests, the bow turns to portside, leading to the global clockwise flow. Both numerical methods capture the counterclockwise rotational flow causing negative Liutex (N.L.1) near the free surface and the clockwise rotational flow that leads to positive Liutex (P.L.1) near the bilge of the bow. The convergence point (C.P.) of counterclockwise and clockwise rotating flow is almost the same. Both flows direct counterclockwise to the hull after confluence. The significant difference between both numerical methods is the distribution of axial Liutex on the starboard of the hull. Posivite Liutex (P.L.3) on the starboard is presented by DDES method not RANS approach. At this point, P.L.3 is mainly concentrated near the free surface.

The next is the distribution of axial Liutex and streamline at $x/L_{pp} = 0.50$. Fig. 11 (a) depicts the global distribution. Currently, the vortex pair 1 (V.P.1) on the portside has shedding from the hull, which includes the positive Liutex 1 (P.L.1) and negative Liutex 1 (N.L.1). There is small difference in the distribution of axial Liutex and streamlines on the portside, which is obtained in both numerical simulations. However, the DDES method captures more stronger vortex pair 3 (V.P.3) on the starboard, as shown in Fig. 11 (b). The curvature of streamlines presented by DDES method is much larger than that in the simulation with RANS approach, which indicates that the intensity of axial Liutex captured by DDES is much larger than that of RANS simulation.

At last, the axial Liutex and streamlines on the cutting plane $x/L_{pp} = 0.90$ which is locating at the stern of the hull are presented in Fig. 12. The vortex pair 1 (V.P.1) corresponding to the positive Liutex 1 (P.L.1) has been far away from the hull and the vortex pair 2 (V.P.2) including the positive Liutex 2 (P.L.2) has been formed at the stern near the hull. Currently, the vortex pair 3 (V.P.3) corresponding to the positive Liutex 3 (P.L.3) and negative Liutex 3 (N.L.3) has been away from the free surface and approaching to the hull at the stern. And V.P.3 is going to merge with V.P.2 downstream. However, this phenomenon is only visible in the results obtained by DDES method.

4.2. Dynamic pure sway test

4.2.1. Force and moments

In this subsection, Fig. 13 depicts the comparison between the predicted and experimental forces and moment in the dynamic pure sway

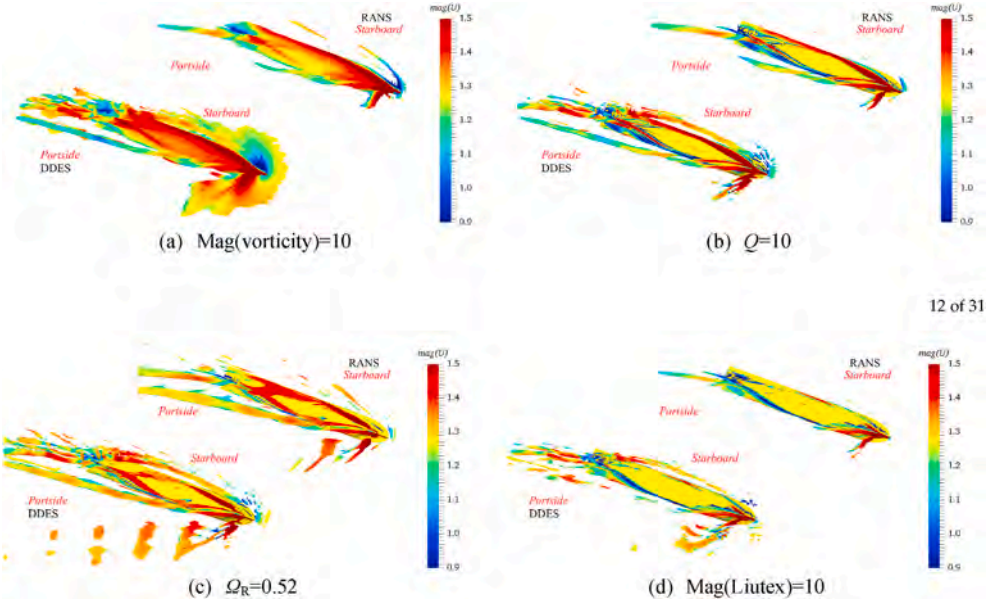

Fig. 9. Vortex structure (a: Mag (vorticity); b: *Q*-criteria; c: ΩR; d: Mag (Liutex)).

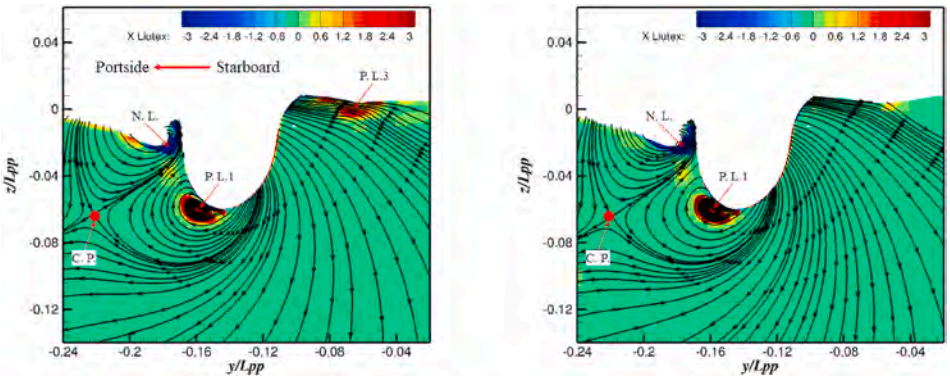

Fig. 10. Distribution of axial Liutex and streamline at $x/L_{pp} = 0.10$ (left: DDES; right: RANS).

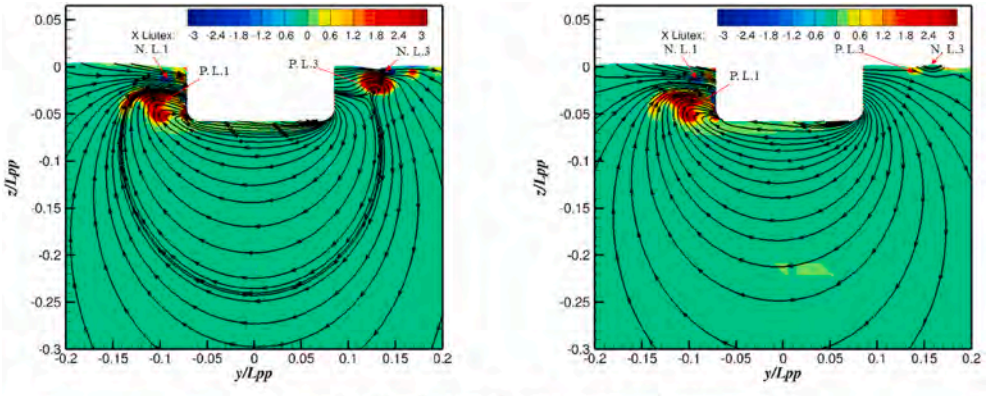

(a) Global distribution of axial Liutex and streamline

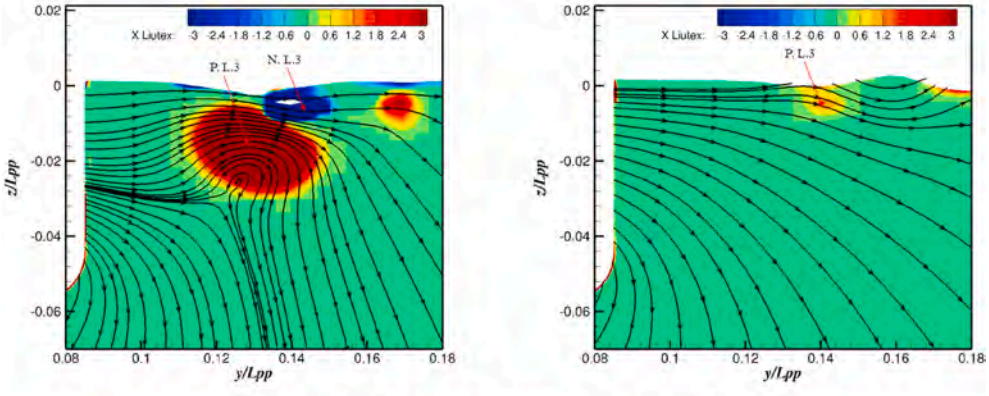

(b) Local view of axial Liutex and streamline

Fig. 11. Distribution of axial Liutex and streamline at $x/L_{pp} = 0.50$ (left: DDES; right: RANS).

test. The left column is the forces/moment and the right is the corresponding vibration frequency obtained by Fast Fourier Transform (FFT). In this part, the error of resistance is obtained by the mean value of its time history. While the error of lateral force and yawing moment is according to the mean values of four magnitudes of their time histories in the plots. This is because that the amplitude of lateral force and yawing moment are difficult to predict accurately. As shown in Fig. 13 (a), there is almost no difference for the time histories of resistance calculated by both numerical methods. However, the resistance in the experiments is more fluctuate, leading to the large error of resistance. As depicted in the plots, the time histories of lateral force and yawing moment obtained by both numerical methods are almost identical, and they are in good agreement with the experimental values except near the peak. The errors between the predicted and experimental data are summarized in Table 7. As shown in the table, the resistance is more under-predicted by DDES method than that with RANS approach. But the errors of lateral force and yawing moment obtained by both methods are little different and even the yawing moment is more accurately predicted by DDES method.

The vibration frequency obtained by FFT is presented in Fig. 13 (b). There is no main frequency of vibration in the time history of the resistance, but there is a second-order frequency oscillation with one period of 4s, which may be induced by the evolution of bow wave during the dynamic motion. The second-order oscillation of resistance mainly comes from numerical oscillation of VOF method. The second-order oscillation also affects the lateral force and yawing moment. However,

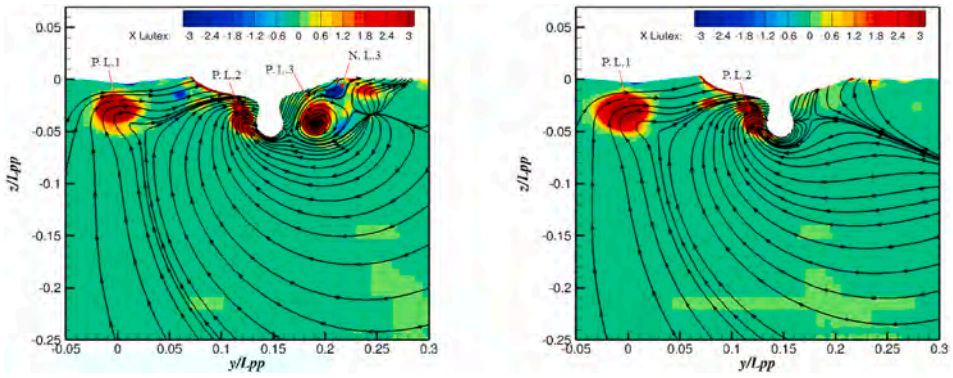

Fig. 12. Distribution of axial Liutex and streamline at $x/L_{pp} = 0.90$ (left: DDES; right: RANS).

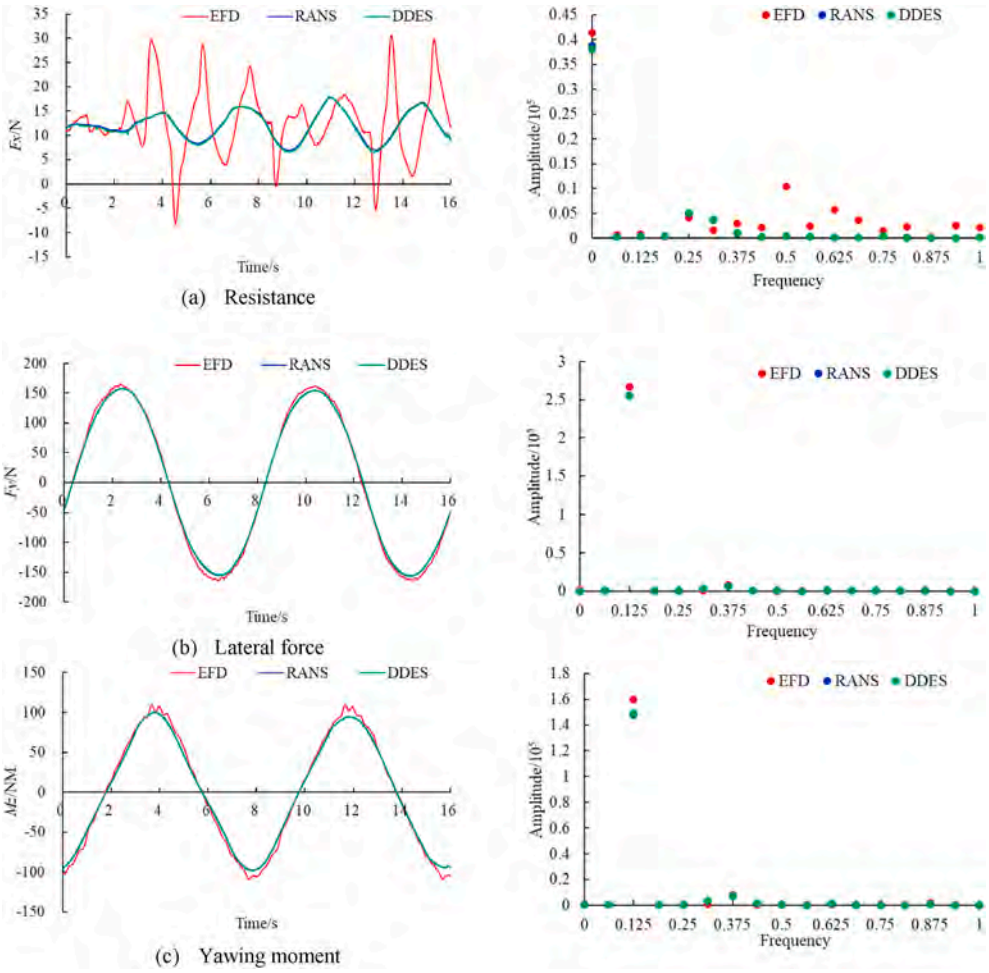

Fig. 13. Forces and moment (left) and Vibration frequency (right).

Table 7
Comparison between calculated and experimental forces and moment in pure sway tests.

Force/moment	EFD	CFD			
		RANS	Error	DDES	Error
Mean of resistance (N)	12.65	12.14	−6.04%	11.87	−8.12%
Amplitude of lateral force (N)	165.61	158.03	−4.57%	157.41	−4.95%
Amplitude of yawing moment (NM)	109.88	99.66	−9.30%	100.25	−8.26%

the lateral force and yawing moment are much larger than the results caused by the numerical oscillation, the second-order oscillation is very little in the FFT results. The dominant vibration frequency of lateral force and yawing moment corresponds to the period 8 s of dynamic pure sway motion. The predicted results of dominant frequency in both numerical simulations agree well with the experimental data.

Table 8 shows the predicted and experimental dimensionless hydrodynamic derivatives in the dynamic pure sway tests. As listed in the table, the predicted derivatives with DDES method of lateral force are less than that obtained by RANS approach with the larger derivatives of yawing moment from DDES model. In generally, the predicted

hydrodynamic derivatives are all less than that in the experiments.

4.2.2. Free surface

Fig. 14 shows the comparison between the evolution of Kelvin wave pattern, turbulent kinetic energy and eddy viscosity coefficient calculated by both numerical methods in one period. Overall, the free surface captured by both methods are similar at different positions. While the turbulent kinetic energy and eddy viscosity coefficients calculated by DDES method are much less than that obtained by RANS approach. In terms of variation trend, not only the free surface but also the distribution of TKE and eddy viscosity coefficient vary periodically with the change of hull lateral position. With the hull moving to portside at T, the flow field on the portside is squeezed, corresponding to an increase of the amplitude of bow wave-making. Currently, there is a relative increase of the amplitude of TKE and eddy viscosity coefficient on the portside.

As shown in Fig. 14 (b), the turbulent kinetic energy calculated by RANS approach is much larger than that in the simulation with DDES method. The TKE obtained by DDES method is mainly concentrated in the Kelvin wave region, while the TKE calculated by RANS approach is mainly distributed around the hull, especially near the bow and stern where the value is much larger than the other region. There is more significant diffidence in the distribution of eddy viscosity coefficient, as presented in Fig. 14 (c). A long-banded region with high eddy viscosity coefficient is particularly prominent in the wake field solved by RANS approach. And in this simulation, the eddy viscosity coefficient near the bow is much larger than that in the other region. But this distribution is obviously unreasonable in the practice. The eddy viscosity coefficient calculated by DDES method is much small but distributes widely in the far field.

4.2.3. Vortex structure

The previous subsection reveals the evolution of free surface and the distribution variation of turbulent kinetic energy and eddy viscosity coefficient on free surface. The following subsection is going to discuss the evolution of vortex structures in the flow field below the free surface.

Here are the vortex structures captured by four vortex identification methods based-vorticity, Q-criteria, Ω_R and Liutex. Fig. 15 shows the vortex structures obtained by DDES and RANS methods. Overall, the DDES method captures more vortex structures than that in the RANS simulations, especially near the bow where large sheet vortex structures on the free surface are visible. But the large sheet vortex structures near the bow are not investigated by Ω_R method, as shown in Fig. 15 (c). It is mainly related to a small positive parameter, ε, to avoid division by zero according to the definition of Ω_R. The main vortex structures in the flow field are obtained by the Ω_R method. Although the vortex structures captured by Q-criteria is like the results calculated by Liutex method, the vortex structures presented by Liutex are unique and directional. Since the vortex structures obtained by the first-generation method-based vorticity, it is obviously unreasonable. In terms of the evolution of the vortex structures in one period, the vortex structures at T and T+2/4 T are basically antisymmetric and they are also antisymmetric at T+1/4 T and T+3/4 T.

At T, a vortex structure originates from the bottom of the bow and shedding from the hull at the shoulder of the hull on the starboard, indicating that the flow separation occurs at the same position. But the vortex structure is clearer in the simulations of DDES method than that with RANS approach. A more significant vortex structure is presented at T+1/4 T. It originates from the bottom at the bow, evolutes along the mid-hull downstream and shedding from the hull at the stern on the starboard. After shedding from the hull, the vortex structure continues to evolute downstream and eventually merges with the vortex structure originating from the propeller shaft. Both numerical methods captured this vortex structure. At T+2/4 T, the distribution of vortex structures are like the results at T, but the vortex structure originating from the bottom of the bow shedding from the bilge on the portside of the hull. The vortex structures at T+3/4 T are analogous to that at T. But the evolution of the vortex structures maintained at T+2/4 T develops in the opposite direction.

Table 8
Predicted and experimental hydrodynamic derivatives.

Hydrodynamic derivatives	EFD	CFD	
		RANS	DDES
Y'_v	1.74e-2	1.66e-2	1.65e-2
$Y'_{\dot{v}}$	2.22e-2	2.12e-2	2.11e-2
N'_v	9.13e-3	8.28e-3	8.33e-3
$N'_{\dot{v}}$	5.79e-4	5.25e-4	5.28e-4

4.2.4. Flow field

Subsection 4.2.4 shows the evolution of axial Liutex and streamlines in the global flow field. However, it is necessary to analyze the flow mechanism at different cutting planes to further understand the flow mechanism. In this subsection, multiple cutting planes are selected to present the distribution of local Liutex and streamline from the bow to the stern.

Fig. 16 presents the details of local flow field at different cutting planes at T when the hull moves from starboard to portside, as indicated by the bold red arrow in Fig. 16 (a). A negative Liutex (N.L.1) is formed at the bottom of the bow on the starboard, where the curvature of streamline is much higher than the other. And more negative Liutex (N.L.) near free surface is captured by DDES method. N.L.1 continues to evolute downstream and appears at the bilge on the starboard at mid-hull, as presented in Fig. 16 (b). In addition to the negative Liutex 1 (N.L.1) on the starboard, there are also negative Liutex occurring at the bilge on the portside and near the longitudinal side. At last, the N.L.1 shed from the hull and gradually separates a positive Liutex (P.L.5) with a very small value, as depicted in Fig. 16 (c). And a negative Liutex (N.L.2) formed near the stern corresponding to the vortex pair 2 (V.P.2) maintained in the previous subsection. In terms of the streamline, the flow is split at the bilge on the portside. In the wake field. In the wake field at $x/L_{pp} = 1.10$, the positive Liutex (P.L.5) that the streamline is clockwise is derived from the N.L.1 and the vortex pair 2 (V.P.2) includes a small positive Liutex 2 (P.L.2) and a large negative Liutex 2 (N.L.2) with the curvature of streamline being great. In general, the distribution of axial Liutex and streamline obtained by RANS approach is like the results by DDES method.

Fig. 16 presents the distribution of axial Liutex and streamlines at the maximum velocity. Next is their distribution at the maximum lateral displacement. The velocity of the hull is close to zero at T+1/4 T, but becomes positive at the next time. The bold red arrow indicates that the hull will move from portside to starboard next time step. At this time, a small negative Liutex 1 (N.L.1) is formed at the bottom of the bow, as displayed in Fig. 17 (a). The flow of each side gathers here and flows far away, as the streamline indicates. In practice, the negative Liutex 1 (N.L.1) gradually splits into a vortex pair that including a week negative Liutex 1 (N.L.1. W) and a week positive Liutex 1 (P.L.1. W), appearing in Fig. 17 (b) and a strong negative Liutex (N.L.1. S) downstream. This phenomenon is captured by both numerical methods and a negative Liutex is also calculated by DDES method. It can also be seen that the clockwise streamline corresponding to the positive Liutex and the counterclockwise is opposite.

During the evolution of axial Liutex and streamline, the strong Liutex (N.L.1. S) gradually sheds from the hull at the bilge and has been far away from the hull at $x/L_{pp} = 0.90$, where the vortex pair 2 (V.P.2) with alternating positive (P.L.2) and negative (N.L.2) Liutex has been initially formed on the portside. In the wake field, the strong negative Liutex (N.L.1. S) is going to merge with the vortex pair 2 (V.P.2) and Fig. 17 (d) proves this phenomenon. Overall, the basic process of the evolution of axial Liutex and streamlines are almost the same obtained by both

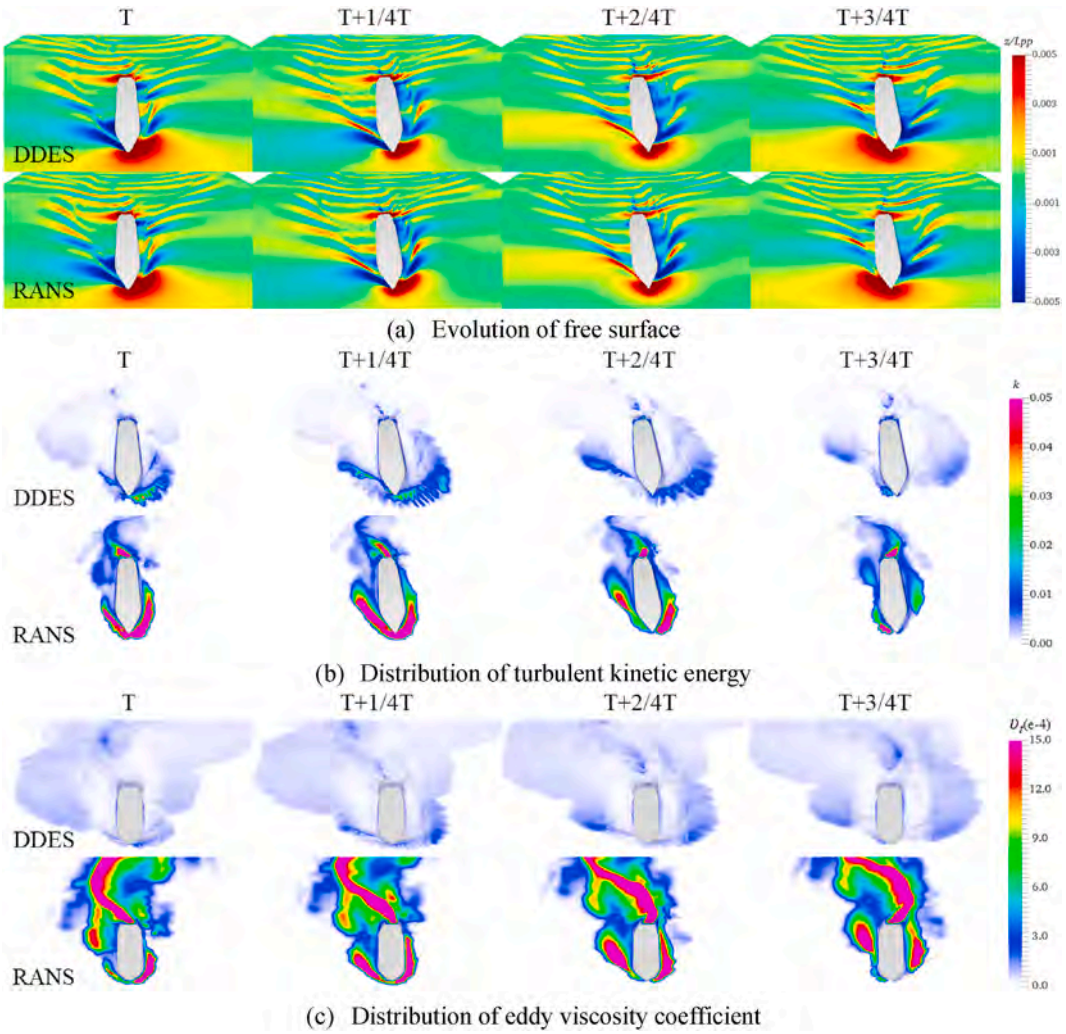

Fig. 14. Evolution of free surface (a), turbulence kinetical energy (b) and eddy viscosity coefficient (c).

numerical methods. And DDES method captures more break Liutex vector in the flow field.

4.3. Dynamic pure yaw test

4.3.1. Force and moments

Since the dynamic pure yaw test is the superposition of static drift test and dynamic pure sway test, the hydrodynamic performance and viscous field flow are more difficult to predict accurately. To evaluate the errors of force and moment, the mean value of the time histories are used for resistance and the amplitudes of their time histories are adopted for the lateral force and yawing moment. The oscillation frequency of the force and moment is analyzed by FFT method.

Fig. 18 and Table 9 show the comparison between force and moment obtained by three method, DDES, RANS and experiment. Different from the results in static drift and dynamic pure sway tests, the resistance is more obviously periodical in the dynamic pure yaw motion. This is mainly due to the periodic variation of the yaw angle. According to the vibration frequency shown in Fig. 18 (b), there is oscillation frequency with one period being 4 s in that the yaw angle varies from maximum to minimum. There is also higher-order oscillation frequency in the experiment, which may be related to the measurement strategy in the experiment. In terms of the lateral force and yawing moment, the predicted results obtained by both numerical methods are in good agreement with experimental data. Their dominant vibration frequency is also the same as the experimental value. Although the second-order frequency oscillation of the lateral force are also accurately predicted by both numerical methods, but bot yawing moment.

Table 9 list the errors of forces and moment in the dynamic pure yaw tests. The yawing moment is more accurately predicted than resistance and lateral force. The lateral force is under-estimated by 15% in both numerical simulations. While the resistance is over-predicted by 14%. The results are acceptable. Table 10 summaries the hydrodynamic derivatives obtained by numerical simulations and experiments. The predicted derivatives by both numerical methods are all less than that in experiments. And the derivatives of lateral force achieved by DDES method are slightly less than that obtained by RANS approach. While the derivatives of yawing moment are slightly larger than that from RANS method.

4.3.2. Free surface

Due to the superposition of yaw motion, the free surface in dynamic pure yaw tests are much more complex than that in dynamic pure yaw test, as depicted in Fig. 19. And the turbulent kinetic energy and eddy viscosity coefficient are presented in Fig. 19 (b) and Fig. 19 (c), respectively. In terms of free surface, the similar results are obtained by both numerical methods. Due to the theory of RANS approach, the free surface captured by it is smoother than that obtained by DDES method.

Similar to the results in the static drift and dynamic pure sway tests, the TKE and eddy viscosity coefficient calculated by RANS are much larger than those by DDES. At T, the lateral displacement of the hull is maximum with the yawing angular velocity being also maximum,

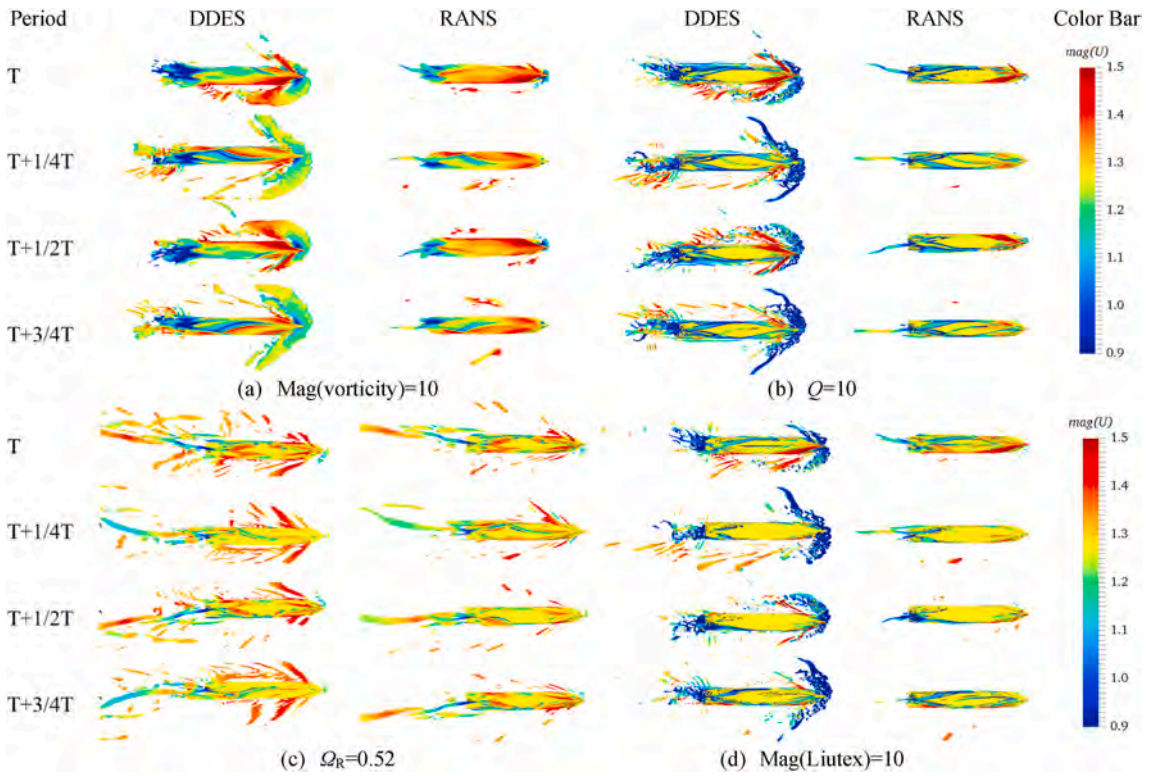

Fig. 15. Comparison of vortex structure obtained by different vortex identification method (a: Mag (vorticity); b: *Q*-criteria; c: Ω_R; d: Mag (Liutex)).

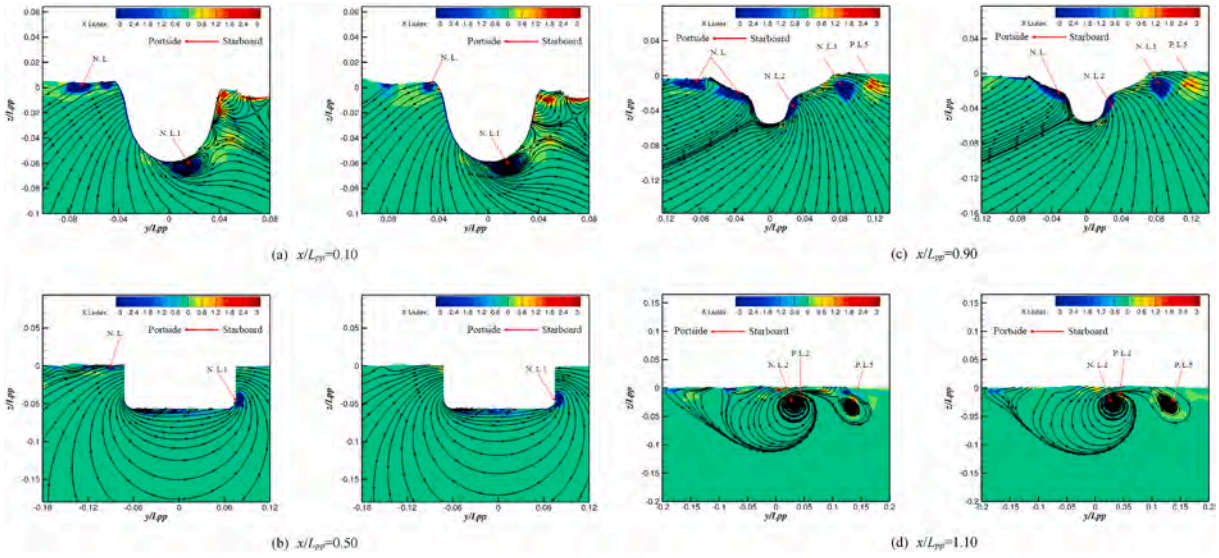

Fig. 16. Distribution of axial Liutex and streamline at different cutting planes at T in the dynamic pure sway tests (left: DDES; right: RANS).

corresponding to the minimum of the lateral velocity and yawing angle. The TKE near the bow, especially on the starboard, is much larger than the other region on the free surface. The more obvious difference of TKE at the bow is presented by RANS calculation, as presented in Fig. 19 (b). Compared with the distribution of TKE in the dynamic pure sway test, the larger region of TKE in the current simulations indicates that the superposition of yaw motion makes the turbulence on the free surface more intense. At T+1/4 T, the absolute of yaw angle and lateral force are the maximum while the minimum are the lateral displacement and yawing angular velocity. In the current, the high TKE mainly concentrates on the starboard and stern of the hull. The distribution of TKE at T+3/4 T is basically anti-symmetrical with the distribution at T.

Compared with the distribution of eddy viscosity coefficient calculated by DDES, the region with high coefficient is mainly concentrated around the hull and the stern on the free surface solved by RANS approach, as shown in Fig. 19 (c). At T+1/4 T, the yaw angle reaches the maximum. It is found that the both sides of the hull are fully covered by the high eddy viscosity coefficient calculated by RANS approach. While the high eddy viscosity coefficient is only distributed near the bow wave and it is very small around the hull in the simulations with DDES method. Obviously, the distribution of eddy viscosity coefficient solved by RANS method is unreasonable.

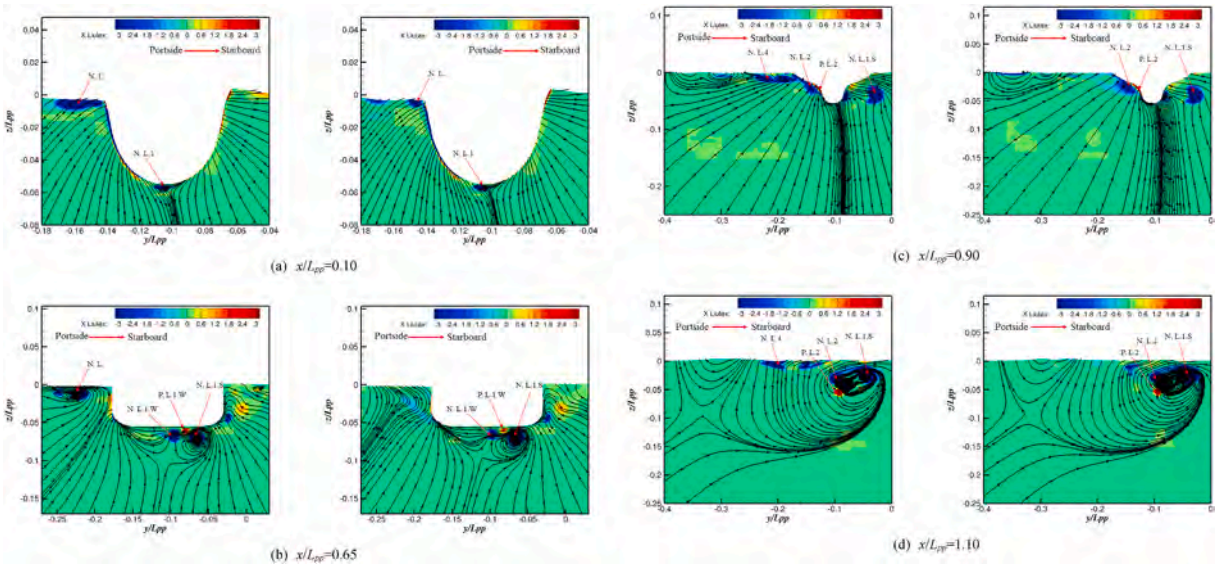

Fig. 17. Distribution of axial Liutex and streamline at different cutting planes at T+1/4 T in the dynamic pure sway tests (left: DDES; right: RANS).

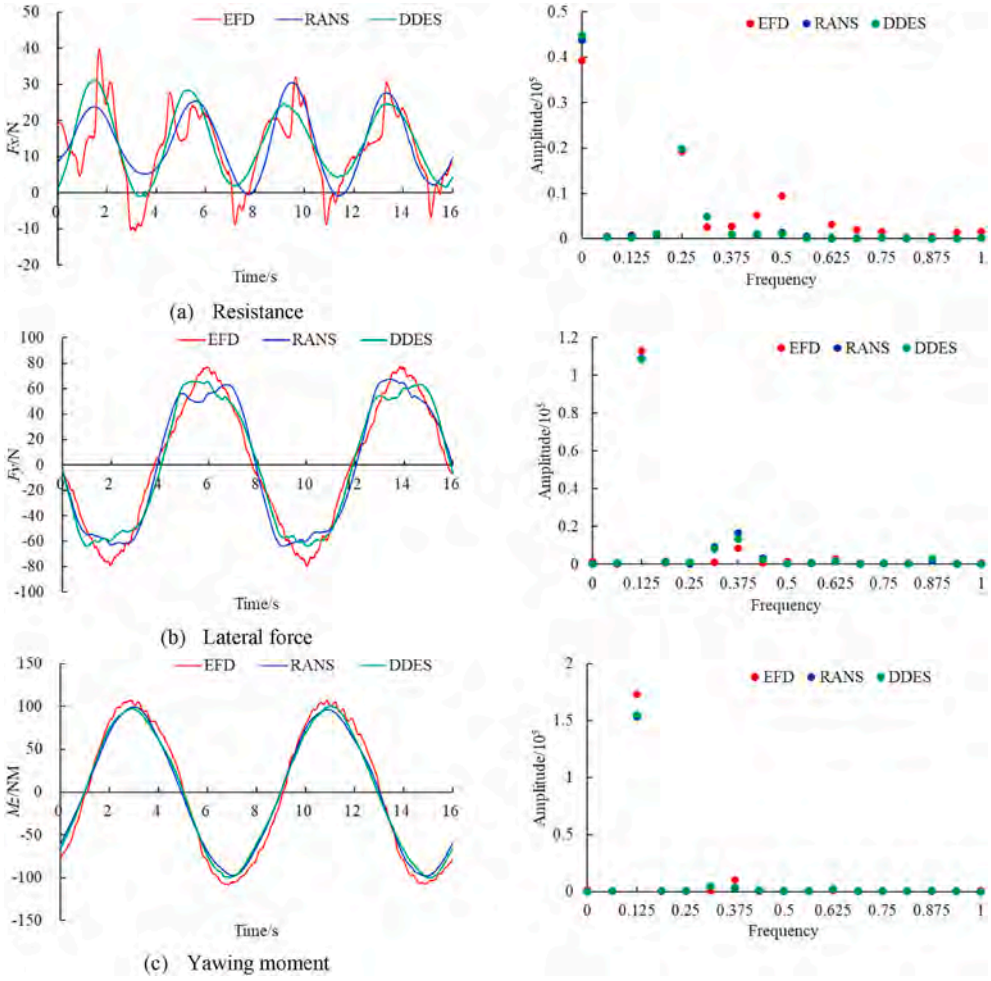

Fig. 18. Forces and moment (left) and Vibration frequency (right).

4.3.3. Vortex structure

By comparing with the vortex structure in dynamic pure sway tests, it is found that large sheet vortex structures near the bow on the free surface are reduced due to the superposition of yaw motion, as depicted in Fig. 20. Only at T and T+1/2 T when the yaw angle of the hull is basically zero, the large sheet vortex structures near the bow are captured by the method based-vorticity in the numerical simulations using DDES model. However, the complex vortex structures near the

Table 9
Comparison between predicted and experimental forces and moment in pure yaw tests.

Force/moment	EFD	CFD			
		RANS	Error	DDES	Error
Mean of resistance (N)	12.75	13.67	11.59%	13.99	14.24%
Amplitude of lateral force (N)	77.78	67.51	−13.21%	65.67	−15.57%
Amplitude of yawing moment (NM)	106.95	99.59	−6.89%	100.47	−6.06%

Table 10
Predicted and experimental hydrodynamic derivatives.

Hydrodynamic derivatives	EFD	CFD	
		RANS	DDES
Y'_v	2.50e-2	2.17e-2	2.11e-2
$Y'_{\dot{v}}$	1.31e-3	1.14e-3	1.11e-3
N'_v	6.78e-3	6.31e-3	6.37e-3
$N'_{\dot{v}}$	2.57e-3	2.40e-3	2.42e-3

bow are also captured by other three methods such as Q-criteria, Ω_R and Liutex. On the other hand, a long vortex structure originating from the propeller shaft was captured by the four vortex identification methods. Overall, the main vortex structures are also able to be captured by RANS method. DDES approach can capture more break and fine vortex structures.

At T, a vortex structure originating from the bulb on the starboard sheds off from the shoulder of the hull and is broken after contacting the hull again downstream. The vortex structure is captured by DDES and RANS methods. Since the hull yaws from starboard to portside at this position, it was difficult for this vortex structure to develop in the far field. At T+1/4 T, the yaw angle reaches the maximum. A vortex structure originates from the bilge on the portside, shedding from the hull approximately at the middle of the hull, and then rapidly splitting into a strong main vortex structure and a weak vortex pair. This phenomenon will be further analyzed in the next. The vortex structures at T+1/2 T and T+3/4 T are the mirror of vortex structures at T and T+1/4 T, respectively.

4.3.4. Flow field

Next is the further analyze of axial Liutex and streamlies on the different cutting planes at T (Fig. 21) and T+1/4 T (Fig. 22). The main vortex structures (V.P.1 and V.P.2) originate from the same position, which is proved by Fig. 21 (a). At this position, it is clearly to investigate the vortex pair 1 (V.P.1), including negative Liutex 1 (N.L.1) and positive Liutex 1 (P.L.1), and V.P.2 which the results of the evolution of the negative Liutex 2 (N.L.2) downstream. In fact, the axial Liutex has been split at this position and they are from the same vortex pair at $x/L_{pp} = 0.05$. In addition, the negative axial Liutex (N.L.3) are also captured by both numerical method near the free surface. In terms of streamlines, the larger curvature of streamlines leads to the greater absolute value of the axial Liutex. The counterclockwise streamlines correspond to the negative Liutex and the clockwise is the positive. The counterclockwise

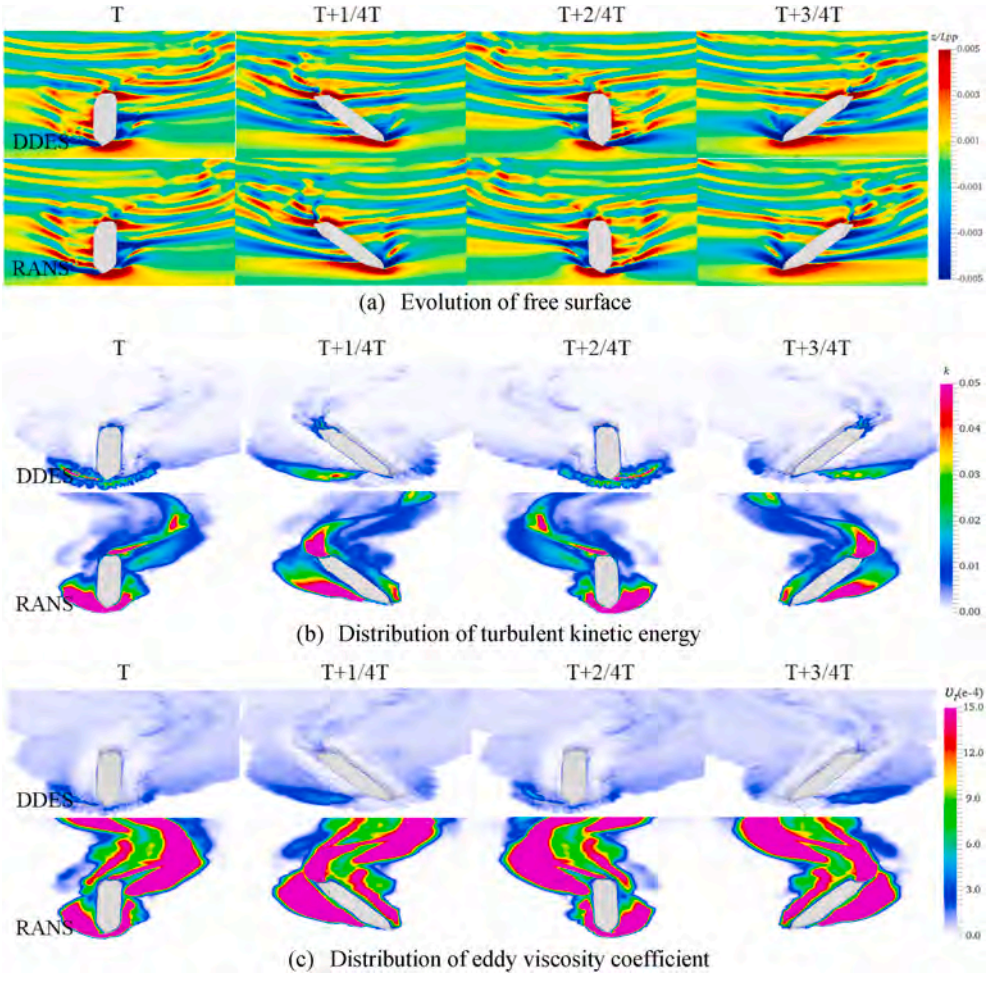

Fig. 19. Evolution of free surface (top), turbulent kinetic energy (middle) and eddy viscosity coefficient (bottom).

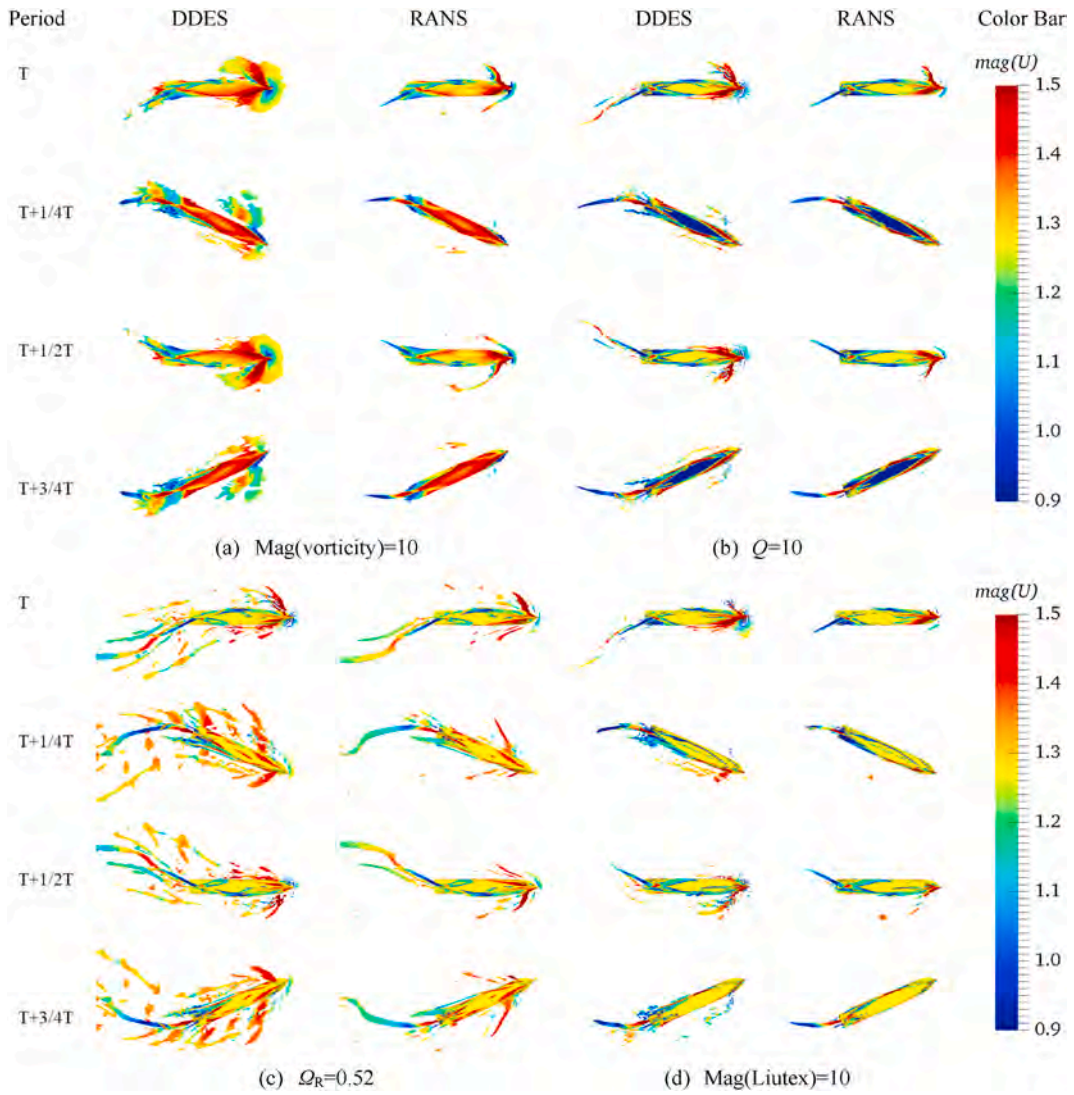

Fig. 20. Vortex structure obtained by different vortex identification method (a: Mag (vorticity); b: *Q*-criteria; c: Ω_R; d: Mag (Liutex)).

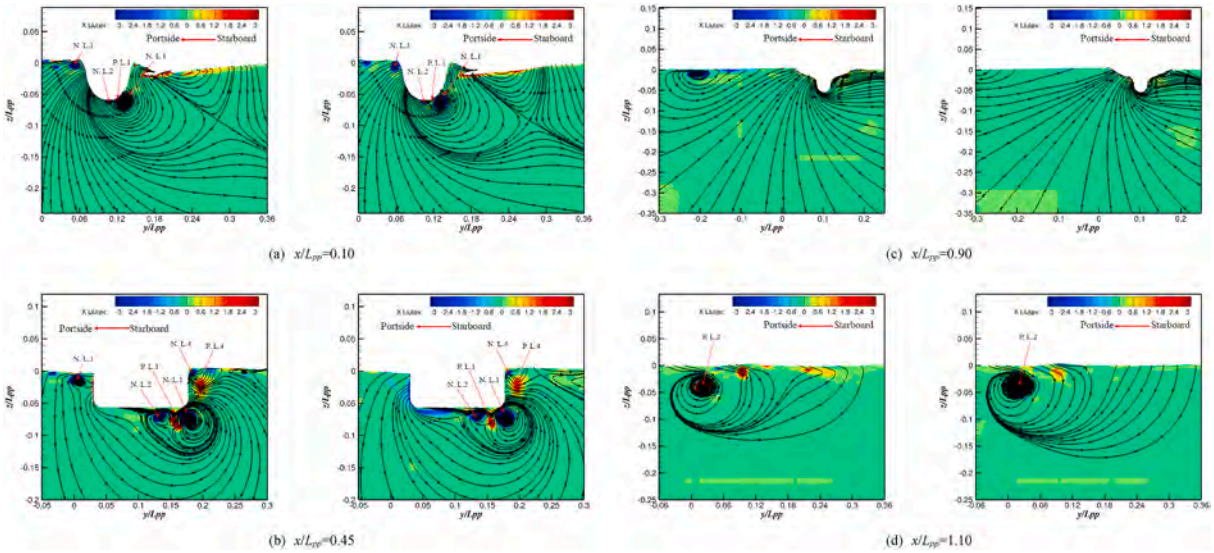

Fig. 21. Distribution of axial Liutex and streamline at different cutting planes at T in the dynamic pure yaw tests (left: DDES; right: RANS).

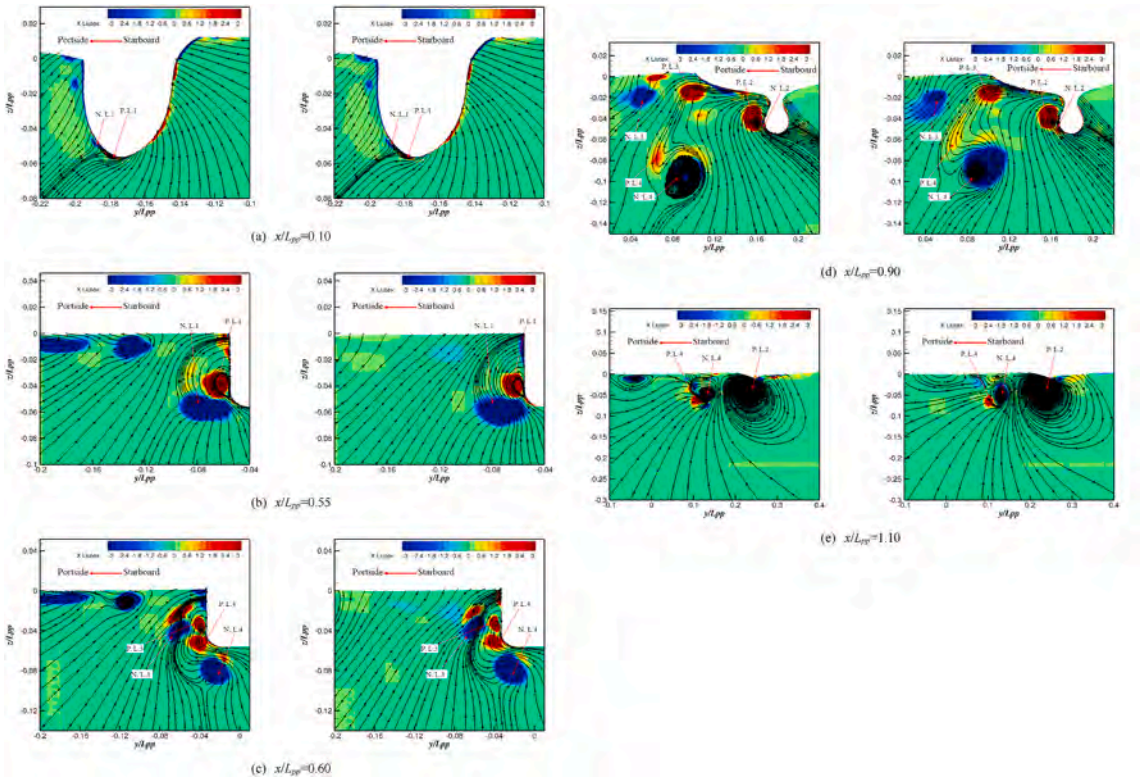

Fig. 22. Distribution of axial Liutex and streamline at different cutting planes at T+1/4 T in the dynamic pure yaw tests.

and clockwise flow converge at about $y/L_{pp} = 0.28$ and $z/L_{pp} = -0.09$.

As the axial Liutex evolutes downstream, the splitting of the vortex structure becomes more and more obvious, as displayed in Fig. 21 (b). The negative axial Liutex 2 (N.L.2) has completely split from the main axial Liutex. And a vortex pair (V.P.1) appears at the bilge on the starboard. While the N.L.3 captured by DDES method is not investigated in the results of RANS simulation, indicating that N.L.3 does not develop to this position in the flow field solved by RANS approach. Interestingly, there is a vortex pair (V.P.4) including N.L.4 and P.L.4 near the free surface. High curvature streamlines are mainly concentrated in the strong vortex region.

At $x/L_{pp} = 0.90$ and 1.10, the distribution of axial Liutex calculated by both methods are similar. It indicates that the vortex structures in front of the hull break and disappear quickly during the evolution downstream. In the wake field, theV.P.2 is the main vortex structure, that is proved in Fig. 21 (d).

Fig. 22 presents the distribution of axial Liutex and streamlines at different cutting planes with the maximum yaw angle. Currently, the vortex structures mainly occur behind the mid-hull. In Fig. 22 (a), the basically same distribution of axial Liutex and streamlines are calculated by both numerical methods. Here starts to form the vortex pair 1 (V.P.1) that contains the negative and positive axial Liutex 1 (P.L.1 and N.L.1). By comparing the distribution of axial Liutex and streamlines in Fig. 22 (b) and Fig. 22 (c), it is found that the vortex pair 1 (V.P.1) at the bilge is rapidly split into the vortex pair 3 and 4 (V.P.3 and V.P.4). In addition, more negative Liutex is calculated by DDES method near the free surface. At $x/L_{pp} = 0.60$, the negative axial Liutex 4 (N.L.4) has shed from the hull. And the V.P.3 and V.P.4 are gradually away from the hull downstream, that have been presented in Fig. 22 (d). The strong vortex pair 2 (V.P.2) has been formed at $x/L_{pp} = 0.90$. But the positive Liutex 4 (P.L.4) has been very weak and is about to disappear. In the wake field, there are only two main vortex structures (V.P.2 and V.P.4), as shown in Fig. 22 (e).

5. Conclusions

To explore the flow mechanism in planar motion mechanism (PMM) tests, the viscous flow field of Yupeng ship is solved by DDES and RANS approaches coupling with dynamic overset gird technology. The time histories of forces/moment acting on the hull are compared with the experimental results. Four vortex identification methods are applied to capture the vortex structures around the hull. In addition, the axial Liutex vector and streamlines on different cutting planes are also analyzed for revealing the flow mechanism around the hull.

Through the comparison between predicted and experimental forces/moments, it is found that the predicted results obtained by DDES and RANS approaches are in good agreement with the experimental data. In the experiment, there is a high-frequency oscillation that is induced by the experimental facility in the time histories of forces/moments acting on the hull. So, the error of resistance is acceptable in the present simulations. In the static drift tests, the resistance is underestimate by DDES and RANS methods with the lateral force being over-predicted. The yawing moment is more accurately estimated by DDES method. In the dynamic tests, the forces/moments and oscillation frequency predicted by DDES and RANS methods are in good agreement with the experimental results. In addition, there is a second-order frequency oscillation found in the results of resistance, that is related to the bow wave-making.

Large turbulent kinetic energy obtained by both methods occurs near the bow and stern, indicating that there is strong turbulent flow. TKE obtained by DDES method is much less than that by RANS approach. However, the evolution region of TKE calculated by DDES method is larger than the results from RANS approach on both side of the hull, indicating that turbulence in the simulation with DDES method develops further in the far-field. The TKE achieved by RANS approach decays rapidly during the development to the far field flow. The turbulent flow is rapidly averaged by RANS method in the far flow field, indicating that RANS method cannot reflect the real flow field. The evolution and distribution of eddy viscosity coefficient are similar to the evolution and

distribution of TKE. This distribution illustrates that there is serious dissipation near the bow and stern of the hull, resulting in the lower velocity in wake field.

By comparing the vortex structures and streamlines in the flow field solved by DDES and RANS methods, it is found that DDES method is more suitable for simulating the large separated flow around the hull. The superposition of yaw motion induces the more intense turbulent flow in the dynamic pure yaw tests than that in dynamic pure sway tests. By analyzing the vortex structures obtained by four vortex identification methods, it is found that Ω_R and Liutex methods (third generation) are suitable for capturing the vortex structures in the large separated flow. Ω_R method is not sensitive with threshold and Liutex is a vector with being unique, accurate, and Galilean invariant. In addition, the third generation of vortex identification methods provide more information such as the vortex boundary, vortex axis and capture weak vortex.

In the next, the static drift test with larger drift angle will be simulated by DDES and RANS. Compared with RANS method, LES approach is more suitable for analyzing the large separated flow around the hull.

Author contributions

Funding acquisition, supervision, Decheng Wan; writing-original draft preparation, Zhen Ren; writing-review and editing, Jianhua Wang; numerical simulations, Zhen Ren; post-processing, Zhen Ren.

Funding**:** This work is supported by the National Natural Science Foundation of China (52131102, 51879159, 51809169). The National Key Research and Development Program of China (2019YFB1704200, 2019YFC0312400), to which the authors are most grateful.

Author statement

Zhen Ren: Data curation, Writing-Original draft preparation, Visualization, Investigation, Software, Validation.

Jianhua Wang: Software, Data curation, Visualization, Investigation, Validation.

Decheng Wan (Corresponding author): Supervision, Conceptualization, Methodology, Investigation, Writing-Reviewing and Editing.

Declaration of competing interest

The authors declare that they have no known competing financial interests or personal relationships that could have appeared to influence the work reported in this paper.

References

Berberović, E., van Hinsberg, N.P., Jakirlić, S., et al., 2009 Mar. Drop impact onto a liquid layer of finite thickness: dynamics of the cavity evolution[J]. Phys. Rev. E - Stat. Nonlinear Soft Matter Phys. 79 (3 Pt 2), 036306.

Bhushan, S., Xing, T., Stern, F., 2012. Vortical structures and instability analysis for Athena wetted transom flow with full-scale validation[J]. J. Fluid Eng. 134 (3), 031201.

Derradji-Aouat, A., Thiel, A.V., 2004. Terry Fox Resistance Tests-phase III (PMM) ITTC Experimental Uncertainty Analysis Iniative[J]. Technical Report.

Heydari, M., Sadat-Hosseini, H., 2020. Analysis of propeller wake field and vortical structures using *k-ω* SST Method[J]. Ocean. Eng. 204, 107247.

Kandasamy, M., Xing, T., Stern, F., 2009. Unsteady free surface wave-induced separation: vortical structures and instabilities[J]. J. Fluid Struct. 25 (2), 343–363.

Liu, C., Gao, Y., Dong, X., et al., 2019. Third generation of vortex identification methods: Ω and Liutex/Rortex based systems[J]. J. Hydrodyn. 31, 205–223.

Meng, Q., Wan, D., 2016. Numerical simulations of viscous flow around the obliquely towed KVLCC2M model in deep and shallow water[J]. J. Hydrodyn. Ser. B 28 (3), 506–518.

Menter, F., Kuntz, M., Langtry, R., 2003. Ten years of industrial experience with the SST turbulence model[J]. Heat Mass Tran. 4.

Ohashi, K., Hino, T., 2009. Flow comparisons of DES, DDES and URANS for a circular cylinder[J]. Ship Technol. Res. 56 (2), 87–92.

Pinto-Heredero, A., Xing, T., Stern, F., 2010. URANS and DES analysis for a Wigley hull at extreme drift angles[J]. J. Mar. Sci. Technol. 15 (4), 295–315.

Ren, Z., Wang, J., Wan, D., August 2018. Numerical Simulation of Ship Bow Wave Breaking Using DES and RANS[C]//the 9th International Conference on Computational Methods (ICCM2018), 06-10, pp. 1001–1012. Rome, Italy.

Sakamoto, N., Carrica, P.M., Stern, F., 2012a. URANS simulations of static and dynamic maneuvering for surface combatant: part 1. Verification and validation for forces, moment, and hydrodynamic derivatives[J]. J. Mar. Sci. Technol. 17 (4), 422–445.

Sakamoto, N., Carrica, P., Stern, F., 2012b. URANS simulations of static and dynamic maneuvering for surface combatant: part 2. Analysis and validation for local flow characteristics[J]. J. Mar. Sci. Technol. 17 (4), 446–468.

Shen, Z., Wan, D., Carrica, P., 2015. Dynamic overset grids in OpenFOAM with application to KCS self-propulsion and maneuvering[J]. Ocean. Eng. 108 (November), 287–306.

Simonsen, C., Stern, F., 2005. Flow pattern around an appended tanker hull form in simple maneuvering conditions[J]. Comput. Fluid 34 (2), 169–198.

Wang, J., Wan, D., 2016. Numerical simulation of pure yaw motion using dynamic overset grid technology[J]. Chin. J. Hydrodyn. 31, 567–574.

Wang, J., Zou, L., Wan, D., 2017. CFD simulations of free running ship under course keeping control[J]. Ocean. Eng. 141, 450–464.

Wang, J., Ren, Z., Wan, D., 2020. Study of a container ship with breaking waves at high froude number using URANS and DDES methods[J]. J. Ship Res. 64 (4), 346–356.

Xing, T., August, 2007. BKW-RS-DES of Unsteady Vortical Flow for KVLCC2 at Large Drift angle[C]//Proc International Conference on Numerical Ship Hydrodynamics, pp. 5–8. Ann Arbor, Michigan.

Xing, T., Stern, M.K.&F., 2007. Unsteady free-surface wave-induced separation: analysis of turbulent structures using detached eddy simulation and single-phase level set[J]. J. Turbul.

Xing, T., Carrica, P., Stern, F., 2010. Large-scale RANS and DDES computations of KVLCC2 at drift angle 0 degree[C]//gothenburg 2010: a workshop on CFD in ship hydrodynamics.

Xing, T., Bhushan, S., Stern, F., 2012. Vortical and turbulent structures for KVLCC2 at drift angle 0, 12, and 30 degrees[J]. Ocean. Eng. 55, 23–43.

Yoon, H., Simonsen, C., Benedetti, L., et al., 2015a. Benchmark CFD validation data for surface combatant 5415 in PMM maneuvers-Part I: force/moment/motion measurements[J]. Ocean. Eng. 109, 705–734.

Yoon, H., Longo, J., Toda, Y., et al., 2015b. Benchmark CFD validation data for surface combatant 5415 in PMM maneuvers-Part II: phase-averaged stereoscopic PIV flow field measurements[J]. Ocean. Eng. 109, 735–750.

Zhao, W., Wan, D., 2016. Detached-Eddy Simulation of Flow Past Tandem Cylinders[J]. Applied Mathematics and Mechanics.

Zhao, W., Zou, L., Wan, D., et al., 2018. Numerical investigation of vortex-induced motions of a paired-column semi- submersible in currents[J]. Ocean. Eng. 164 (SEP.15), 272–283.